1-1-2019

Lotus rhizome-like S/N-C with embedded WS2 for superior sodium storage

Xiu Li
University of Wollongong, Chinese Academy of Sciences, xl816@uowmail.edu.au

Yonggang Sun
Chinese Academy Of Sciences

Xun Xu
University of Wollongong, xun@uow.edu.au

Yunxiao Wang
University of Wollongong, yunxiao@uow.edu.au

Shulei Chou
University of Wollongong, shulei@uow.edu.au

See next page for additional authors

Lotus rhizome-like S/N-C with embedded WS2 for superior sodium storage

Abstract

Sodium-ion batteries (SIBs) hold great promise as power sources because of their low cost and decent electrochemical behavior. Nevertheless, the poor rate performance and long-term cycling capability of anode materials in SIBs still impede their practical application in smart grids and electric vehicles. Herein, we design a delicate method to embed WS2 nanosheets into lotus rhizome-like heteroatom-doped carbon nanofibers with abundant hierarchical tubes inside, forming WS2@sulfur and nitrogen-doped carbon nanofibers (WS2@S/N-C). The WS2@S/N-C nanofibers exhibit a large discharge capacity of 381 mA h g-1 at 100 mA g-1, excellent rate capacity of 108 mA h g-1 at 30 A g-1, and a superior capacity of 175 mA h g-1 at 5 A g-1 after 1000 cycles. The excellent performance of WS2@S/N-C is ascribed to the synergistic effects of WS2 nanosheets, contributing to larger interlayer spacing, and the stable lotus rhizome-like S/N-C nanofiber frameworks which alleviate the mechanical stress. Moreover, the WS2@S/N-C electrode shows obvious pseudocapacitive properties at 1 mV s-1 with a capacitive contribution of 86.5%. In addition, density functional theory calculations further indicate that the WS2@S/N-C electrode is very favorable for Na storage. This novel synthetic strategy is a promising method for synthesizing other electrode materials for rechargeable batteries in the future.

Keywords

rhizome-like, s/n-c, embedded, lotus, ws2, storage, superior, sodium

Disciplines

Engineering | Physical Sciences and Mathematics

Publication Details

Li, X., Sun, Y., Xu, X., Wang, Y., Chou, S., Cao, A., Chen, L. & Dou, S. (2019). Lotus rhizome-like S/N-C with embedded WS2 for superior sodium storage. Journal of Materials Chemistry A, 7 (45), 25932-25943.

Authors

Xiu Li, Yonggang Sun, Xun Xu, Yunxiao Wang, Shulei Chou, Anmin Cao, Libao Chen, and Shi Xue Dou

Lotus Rhizome-like S/N-C for Strengthening WS_2 with Superior Sodium Storage

Xiu Li,[a, b] Yonggang Sun,[b] Xun Xu,[a,*] Yunxiao Wang,[a,*] Shulei Chou,[a] Anmin Cao,[b] Libao Chen,[c,*] and Shixue Dou[a]

[a]*Institute for Superconducting and Electronic Materials, University of Wollongong, Wollongong, NSW 2500, Australia.*

[b]*Key Laboratory of Molecular Nanostructure and Nanotechnology and Beijing National Laboratory for Molecular Sciences, Institute of Chemistry, Chinese Academy of Sciences (CAS), Beijing 100190, P. R. China*

[c]*State Key Laboratory of Powder Metallurgy, Central South University, Changsha, Hunan 410083, P. R. China*

Corresponding authors: Xun Xu, Yunxiao Wang andLibao Chen

Email: xun@uow.edu.au (Dr. X. Xu);

yunxiao@uow.edu.au (Dr. Y. Wang)

lbchen@csu.edu.cn (Prof. L. Chen)

Abstract

Sodium-ion batteries (SIBs) hold great promise as power sources because of their low cost and decent electrochemical behavior. Nevertheless, the poor rate performance and long-term cycling capability of anode materials in SIBs still impede their practical applications in smart grids and electric vehicles. Herein, we design a delicate method to embed WS_2 nanosheets into lotus rhizome-like heteroatom-doped carbon nanofibers with abundant hierarchical tubes inside, forming WS_2@sulfur and nitrogen-doped carbon nanofibers (WS_2@S/N-C). The WS_2@S/N-C nanofibers exhibit a large discharge capacity of 381 mA h g^{-1} at 100 mAg^{-1}, excellent rate capacity of 108 mA h g^{-1} at 30 A g^{-1}, and a superior capacity of 175 mA h g^{-1} at 5 Ag^{-1} after 1000 cycles. The excellent performance of WS_2@S/N-C is ascribed to the synergistic effects of WS_2 nanosheets, contributing to larger interlayer spacing, and the stable lotus rhizome-like S/N-C nanofiber frameworks to alleviate the mechanical stress. Moreover, the WS_2@S/N-C electrode **shows** an obvious pseudocapacitance property at 1 mV s^{-1} with a capacitive contribution of 86.5%. In addition, the density functional theory calculations further indicate that WS_2@S/N-C electrode is very favorable for Na storage. This novel synthetic strategy is a promising method for synthesizing other electrode materials for rechargeable batteries in the future.

Keywords: Tungsten disulfide; carbon; doping; anode; sodium-ion batteries

1. Introduction

Sodium-ion batteries (SIBs) have promisingly replaced for lithium-ion batteries (LIBs) as power sources for smart grids and low-speed electric vehicles, owing to the low cost and abundance of sodium (Na) resources and their high safety due to the high potential of Na (-2.714 V).[1-3] Nevertheless, the radius of Na-ions (1.06 Å) is larger than that of lithium (Li) ions (0.76 Å), leading to sluggish diffusion kinetics for Na^+, making it difficult to find appropriate anode materials with larger interlayer spacing and good reversible Na^+ storage for SIBs.[4, 5] So far, a large number of a node materials have been explored for SIBs, including carbonaceous materials,[6-8] alloying reaction metals and alloys (Sn, Sb, Bi, and their alloys),[9-12] metal oxides[13-15] and chalcognides,[16-18] and others. Among them, carbonaceous materials usually exhibit excellent cycling performance, although they possess relatively low capacity.[19-21] The alloyed metal materials always show high theoretical capacity, but the large volume change problem during the alloying/de-alloying process leads to poor rate capability.[22] In addition, the large volume expansion for Na^+ storage due to the formation of Na_2O and Na_2S (or Na_2Se)[23-26] will shorten the cycling life of these anode compounds. Therefore, it is essential to find effective strategies to obtain excellent anode materials with well-balanced performance in terms of high capacity, excellent rate capability, and long-term cycling stability.

two-dimensional (2D) transition-metal dichalcogenides (TMDCs) have obtained great interest as anode materials for SIBs due to their unique layered structure.[27, 28] As one example of typical TMDCs, tungsten disulfide (WS_2) exhibits larger layer spacing with weak van der Waals interaction and higher electrical conductivity than the traditional MoS_2.[29] Benefiting from its structural characteristics and conductive nature, the WS_2 anode material exhibits high rate capability for SIBs,[30-33] although the long-term cycling performance of WS_2 as anode for SIBs is not satisfactory for practical application. [34] Actually, this is a common issue for metal sulfides as electrode materials for LIBs and SIBs because the cycling life is strongly influenced by certain factors,[34-36] *i.e.*, the large volume changes during electrochemical processes, the Li^+/Na^+ diffusion kinetics, and the obvious dissolution of the polysulfide intermediates. Thus, it is desirable to look for effective means to solve the problem of WS_2 as anode material, endowing it with stable long-term cycling and high rate capability.

Carbon scaffolds have been employed to effectively host metal sulfides as electrode

materials,[37-39] *i.e.*, one-dimensional (1D) carbon nanofibers, graphene, or mesoporous carbon. Among them, the carbon nanofibers have been demonstrated to be a good substrate for hosting metal sulfides as anode materials.[40-44] First, their highly conductive nature, along with the large longitudinal aspect ratio of carbon nanofibers could facilitate electron transfer among the metal sulfide particles and improve the Na^+ diffusion kinetics at the same time, resulting in high rate capability for electrodes. Second, carbon nanofibers can alleviate the mechanical stress during the electrochemical process and prevent the pulverization of the embedded metal sulfide materials, which can yield electrodes that have stable long cycling performance. Last but not least, heteroatom doping is favorable to improve the capacity of carbon nanofibers as electrodes, which can be easily prepared by electrospinning. Based on the above analysis, it would be a promising method to achieve enhanced sodium storage performance with large capacity, excellent rate capability, and cycling stability by embedding WS_2 nanosheets in heteroatom doped carbon nanofibers.

Herein, we have designed a novel method to prepare lotus rhizome-like WS_2@S/N-co-doped carbon nanofibers (denoted as WS_2@S/N-C) to realize the above targets. The synthetic procedures are shown in **Scheme 1**. The WO_3 nanosheets are first synthesized via the hydrothermal method, and then embedded into polymer nanofibers via electrospinning. Subsequently, WS_2@S/N-C nanofibers are obtained through carbonizing the WO_3/poly-acrylonitrile/polymethyl methacrylate (PAN/PMMA) nanofibers with sulfur, with the process including preheating at 230 ^oC and further annealing at 600 ^oC. The designed WS_2@S/N-C nano-architecture offers various advantages: i) the embedding of WS_2 nanosheets in carbon nanofibers could enhance the overall electrode conductivity, offering high accessible capacity; ii) the formation of lotus rhizome-like carbon nanofibers could facilitate electron transfer and prevent the pulverization of the electrode structure, resulting in a stable long-term cycling life span. The WS_2@S/N-C electrode presents a high rate capacity of 108 mA h g^{-1} at 30 A g^{-1}, a good reversible capacity of 321 mA h g^{-1} at 100 mA g^{-1} (*vs.* 25 mA h g^{-1} for WS_2) after 100 cycles, and a stable capacity of 175 mA h g^{-1} at 5 A g^{-1} after 1000 cycles. In addition, both the kinetics calculations and the theoretical analysis demonstrate that S/N-C nanofibers could improve the rate capability of WS_2 materials.

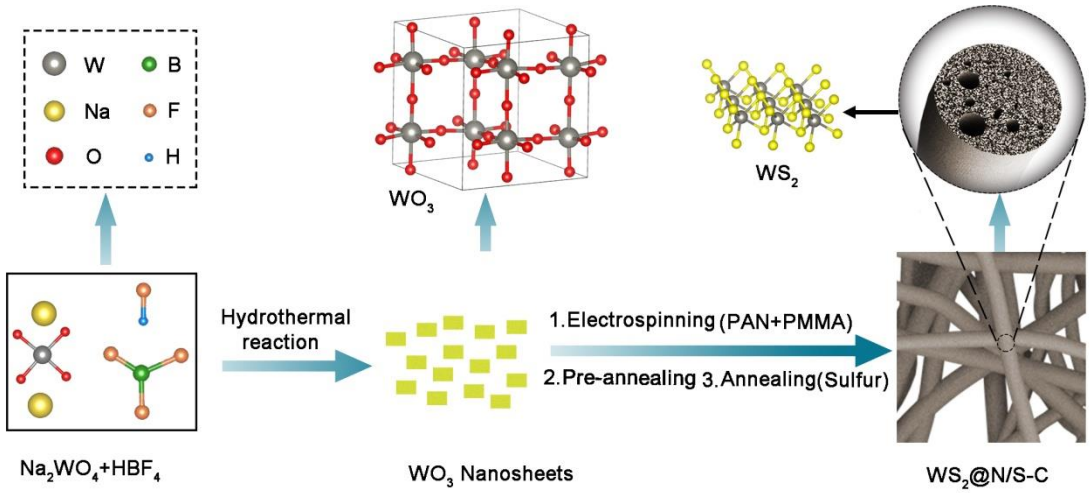

Scheme 1. Schematic illustration of the synthetic route to prepare the porous WS_2@S/N-C nanofibers.

2 Experimental section

2.1 Synthesis of WO_3 nanosheets

WO_3 nanosheets were synthesized according to the literature with minor modification.[45] Typically, 1.0 g $Na_2WO_4 \cdot 2H_2O$ was first dissolved in 40 mL water, and then 3.0 mL HBF_4 solution (40% by weight) was dropped into the solution. After that, the mixture was maintained under hydrothermal conditions at 100 °C for 10 h. Finally, the resulting product was collected with distilled water and absolute ethanol to obtain the pure WO_3.

2.2 Synthesis of WS_2@S/N-C nanofibers

The WS_2@S/N-C nanofibers were produced through the electrospinning method. In a typical synthesis, 0.24 g PMMA and 0.36 g PAN were firstly dissolved in 5 mL dimethylformamide (DMF) solution under vigorous stirring at 60 °C for 4 h. Then, 0.3g as-synthesized WO_3 were added in the above solution to obtain a stable suspension for the electrospinning with an applied voltage of 13 kV and a feeding rate of 0.3 mL h^{-1}. Moreover, the distance between the stainless steel needle and the collector was set to be 15 cm. To stabilize the structure, the obtained fiber-like membrane was annealed at 230 °C for 2 h in air. The pretreated nanofibers were further carbonized with sulfur powder (mass ratio of 1:4) in flowing Ar. The nanofibers and sulfur were carbonized at 600 °C for 2 h to transform the WO_3 into WS_2 in carbon nanofibers.

For comparison, 0.3 g WO_3 and 1.2 g sulfur power were further carbonized by the same method to transform the WO_3 into WS_2. In addition, S/N-C nanofibers were synthesized according to the similar procedure without WO_3 precursor.

2.3 Material characterizations

The morphologies and structure of the as-synthesized samples were measured by field emission scanning electron microscopy (FE-SEM, Helios Nanolab G3UC) equipped with Energy Dispersive Spectrometer (EDS) and field emission transmission electron microscopy (TEM, FEI Titan G2 60–300). The crystal structure and phase composition were confirmed by X-ray powder diffraction (XRD, Rigaku D/Max-2500). Raman spectroscopy (DXR microscope, Thermo Fischer DXR) was carried out with 532 nm laser as excitation resource. Fourier transform infrared spectra were also collected (FT-IR, Nicolet-460). Thermogravimetric analysis (TGA, SDTQ600) was used to confirm the content of WS_2 in the composite. The chemical states of the samples were investigated by X-ray photoelectron spectroscopy (XPS, Escalab 250Xi). Nitrogen adsorption and desorption isotherms (BET, Tristar 3020) was used to determine the Brunauer-Emmett-Teller (BET) surface area.

2.4 Electrochemical measurements

All the electrochemical tests were carried out using 2025 coin-type half cells. The working electrodes were prepared by mixing the active material powder, acetylene black, and carboxymethyl cellulose (CMC) in a weight ratio of 8:1:1 to form a slurry, which was then spread onto Cu foil, subsequently dried in a vacuum oven at 60°C for 12 h, and then cut into 12 mm-diameter discs. The mass loading amount of the active material was about 0.7-0.8 mg cm^{-2}. Half cells were made up using Na metal as the counter electrode and glass fiber as the separator were assembled in an Ar-filled glove box. The electrolyte was 1 M $NaClO_4$ dissolved in a mixture of ethylene carbonate (EC) and diethyl carbonate (DEC) (1: 1 by volume ratio) with 5 wt% fluoroethylene carbonate (FEC). The galvanostatic charge/discharge tests were performed on a battery test system (Land CT2001A), and the cyclic voltammetry (CV) was carried out on an electrochemical workstation (CHI660E), both in the voltage range of 0.01–3 V. All the electrochemical tests were conducted at room temperature.

2.5 Calculation details

To investigate the reasons for the enhanced sodium storage performance, density functional theory

(DFT) calculations were used to investigate the adsorption behavior of Na on the pristine WS_2 and WS_2 with N/S-doped graphene (WS_2/NS@graphene) by using the Vienna Ab-initio Simulation Package (VASP).[46, 47] The exchange-correlation functional,were determined by the generalized gradient approximation (GGA) with the Perdew-Burke-Ernzerhof (PBE) form.[48] The frozen-core projector-augmented wave (PAW) method[49, 50] was used for interactions between the core electrons and the valence electrons. The convergence criterion was set at 10^{-5} eV, and atomic positions were allowed to move until the forces acting on each atoms were less than 0.02 eV/Å for the total energy calculations, with a high energy cut-off of 520 eV. The Brillouin zone was integrated with 3 × 3 × 1 Monkhorst-Pack k-point grids for geometry optimization. Moreover, The vacuum space of 20 Å was used in the z-direction could avoid any interaction between the adjacent repeating layers.

The adsorption energy (E_{ad}) of at Na atom sites in WS_2 and WS_2 with N, S doped graphene (WS_2/NSG) was calculated as follows:

$$E_{ad} = E_{\mathrm{WS2-Na,WS2/NSG-Na}} - E_{\mathrm{WS2,WS2/NSG}} - E_{Na}$$

Where $E_{\mathrm{WS2-Na,WS2/NSG-Na}}$ is the total energy for one Na atom in WS_2 and WS_2/NSG; $E_{\mathrm{WS2,WS2/NSG}}$ is the total energy for WS_2 and WS_2/NSG without the adsorption of Na; $E_{Na}$is for one Na atom in the same slab.

Herein, both the interaction between WS_2 or WS_2/NSG and a Na ion indicates massive charge transfer, which can be visualized by three-dimensional charge difference mapping, and the definition is as follow:

$$\Delta\rho = \rho_{\mathrm{WS2-Na,WS2/NSG-Na}} - \rho_{\mathrm{WS2,WS2/NSG}} - \rho_{Na}$$

Where $\rho_{\mathrm{WS2-Na,WS2/NSG-Na}}$is the charge density of the composite or WS_2 with one Na atom adsorbed; $\rho_{\mathrm{WS2,WS2/NSG}}$is the charge density of the composite or WS_2 without Na; $\rho_{Na}$is the charge density of one Na atom in the same slab, respectively.

3 Results and discussion

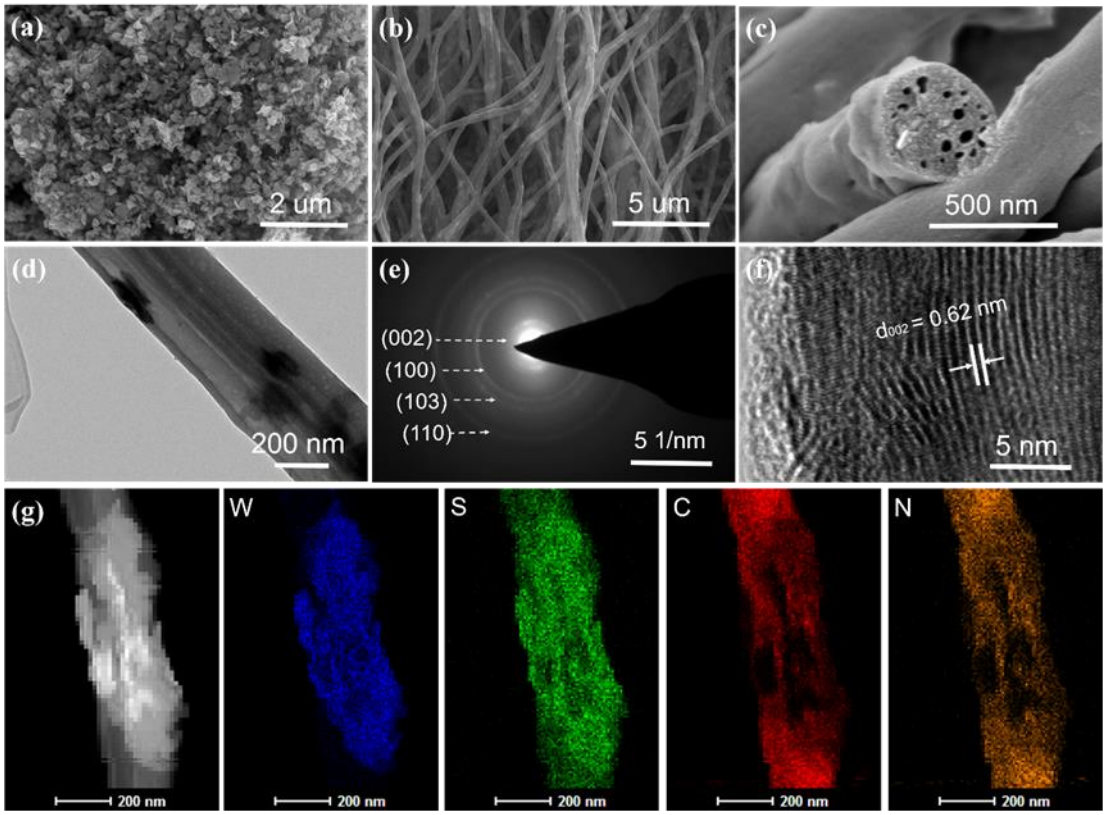

Figure 1 (a) Low–resolution SEM image of WO_3 nanosheets; (b) low–resolution and (c) high–resolution SEM images, (d) low–resolution TEM image, (e) electron diffraction pattern, (f) high–resolution TEM image, and (g) element mapping of WS_2@ S/N-C.

The structure and morphology of the samples were investigated by SEM and TEM, The SEM image in **Figure 1a** exhibits the as-synthesized WO_3 nanosheets with about 40 nm in size, which could be electrospun into PAN/PMMA, and further changed into WS_2@S/N-C nanofibers through a carbonization and sulfidation process. In **Figure 1b**, WS_2@S/N-C nanofibers exhibit a length of several tens micrometers and a diameter of 400 nm. The WS_2@S/N-C nanofibers in **Figure 1c** are observed to be porous like lotus rhizomes due to the decomposition of PMMA during the carbonization process. The embedding could prevent the aggregation of WS_2 nanosheets (**Figure S1a** and **b** in the Supporting Information) during the sulfidation process. In **Figure 1d**, there are some dark parts in the single nanofiber owing to the presence of WS_2 nanosheets embedded in the carbon nanofibers. The selected area electron diffraction (SAED) pattern of WS_2 nanosheets in the WS_2@S/N-C nanofibers is shown in **Figure 1e**. The diffraction rings from inside to outside are attributed to the (002), (100), (103), and (110) planes, respectively. The high-resolution TEM

(HRTEM) image of the vertically grown WS_2 nanosheets in **Figure 1f** displays a 0.62 nm interlayer spacing, which can be attributed to the (002) planes of hexagonal WS_2, consistent with the XRD results for WS_2@S/N-C. This value is in accord with the theoretical interlayer spacing along the *c*-axis direction. The pure WS_2 shows similar results in **Figure S1c** and **d**. The energy dispersive X-ray (EDX) element mapping images indicate that the W, S, C, and N elements are not uniformly distributed throughout the WS_2@S/N-C nanofiber (**Figure 1g**), which is due to the distribution of the isolated nanosheets.

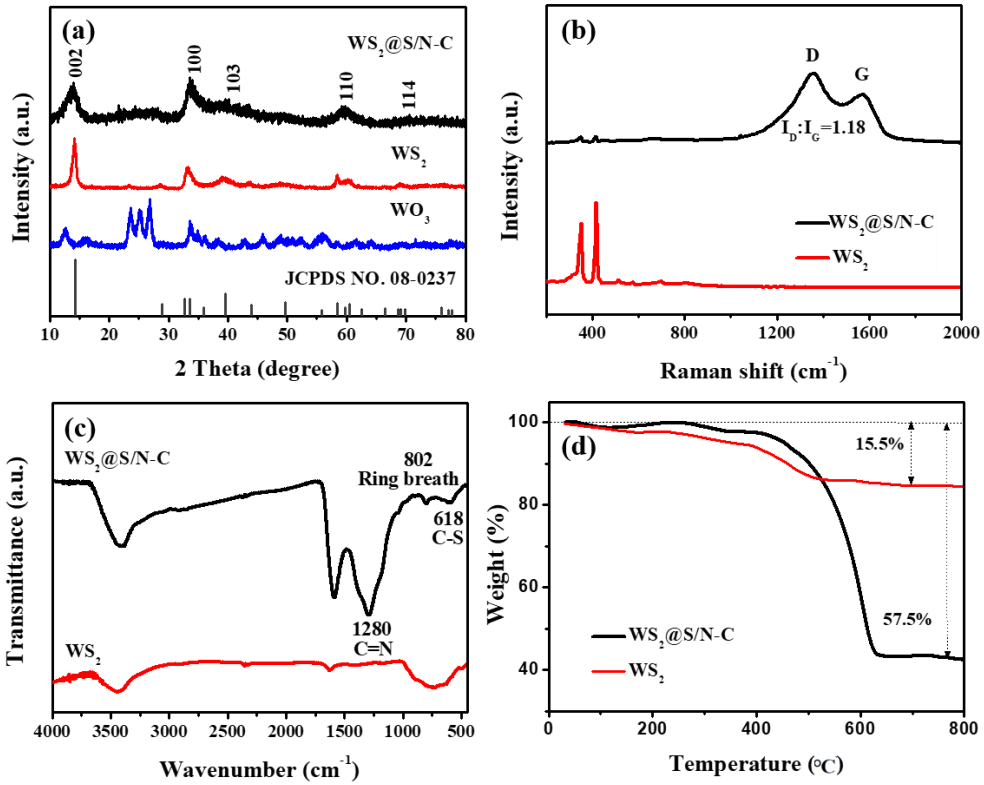

Figure 2 (a) XRD patterns of WO_3, WS_2, and WS_2@S/N-C; (b) Raman spectra, (c) FT-IR spectra, and (d) TGA curves of WS_2 and WS_2@S/N-C.

The components and crystalline phases of the materials were characterized by the XRD. **Figure 2a** compares the XRD patterns of the WO_3, WS_2, and WS_2@S/N-C samples. The diffraction peaks of the pristine WO_3 can be well assigned to a monoclinic phase, and the phase transition from monoclinic WO_3 to hexagonal WS_2 accompanies the carbonization of WO_3 with sulfur to develop WS_2. Strong peaks located at 14.3, 32.76, 39.5, 58.4, and 66.5° can be indexed to the (002), (100), (103), (110), and (114) planes of the hexagonal structure of WS_2 (JCPDS no. 08-0237), respectively. Moreover, the obviously weaker intensity of WS_2@S/N-C compared to the WS_2

implies that the sample was successfully wrapped by carbon nanofibers, which may have restricted the volume changes, preventing the pulverization of the electrode structure over a long-term cycling lifespan. Further structural information on the WS_2@S/N-C and WS_2 was acquired by Raman spectroscopy and FTIR analysis. The peaks of the WS_2 and WS_2@S/N-C samples in the Raman spectra (**Figure 2b**) are located at 351 and 416 cm^{-1}, and can be ascribed to the Raman active E_{2g} and A_{1g} vibration modes for WS_2. [33] Compared to the WS_2, there is weaker intensity for WS_2@S/N-C due to the wrapping with carbon nanofibers. The peaks around 1350 and 1560 cm^{-1} are attributed to the disorder-induced D band and the graphitic G band for the WS_2@S/N-C sample, respectively. In addition, the intensity ratio of the D-band to G-band (1.3, I_D:I_G) implies that more defects exist in WS_2@S/N-C, which is associated with the N, S-co-doping.[51] In the FTIR spectrum of WS_2@S/N-C (**Figure 2c**), three new bands at 618, 802, and 1280cm^{-1} can be respectively attributed to C–S stretching, ring breathing (main-chain hexahydric-ring), and C=N symmetric stretching modes.[52, 53] The observation of C−S bonds confirmed that the S was bonded with S/N-C, which can afford a superior reversible capacity.[54]

The content of WS_2 in the WS_2@S/N-C sample from room temperature to 800 ℃ in air was confirmed by TGA analysis (**Figure 2d**). A weight loss of 14.5% was observed for pure WS_2 due to the oxidation of WS_2 into WO_3. The weight loss (57.5%) for the WS_2@S/N-C sample is associated with the combination of oxidation of WS_2 and combustion of S/N-C. The content of WS_2 in the WS_2@S/N-C sample was calculated to be 45.4 wt%. Moreover, Based on the nitrogen adsorption and desorption isotherms, the Brunauer-Emmett-Teller (BET) surface areas of WS_2 and WS_2@S/N-C samples were found to be 17.74 and 23.4 m^2 g^{-1}, as shown in **Figure S2**. Furthermore, S/N-C nanofibers were also characterized by XRD, SEM, TEM, HRTEM, as shown in **Figure S3a-d**. XRD pattern in **Figure S3a** indicates S/N-C sample is typical carbon material, without other impurities. The sample in SEM and TEM images (**Figure S3b** and **c**) shows porous nanofibers with a length of several tens of micrometers. The amorphous nature of S/N-C sample is confirmed by HR-TEM image in **Figure S3d**. In addition, the content of sulfur doping in the carbon of WS_2@S/N-C and S/N-C samples is confirmed to be ~4.8% and ~6% by EDS (**Figure S4**), respectively.

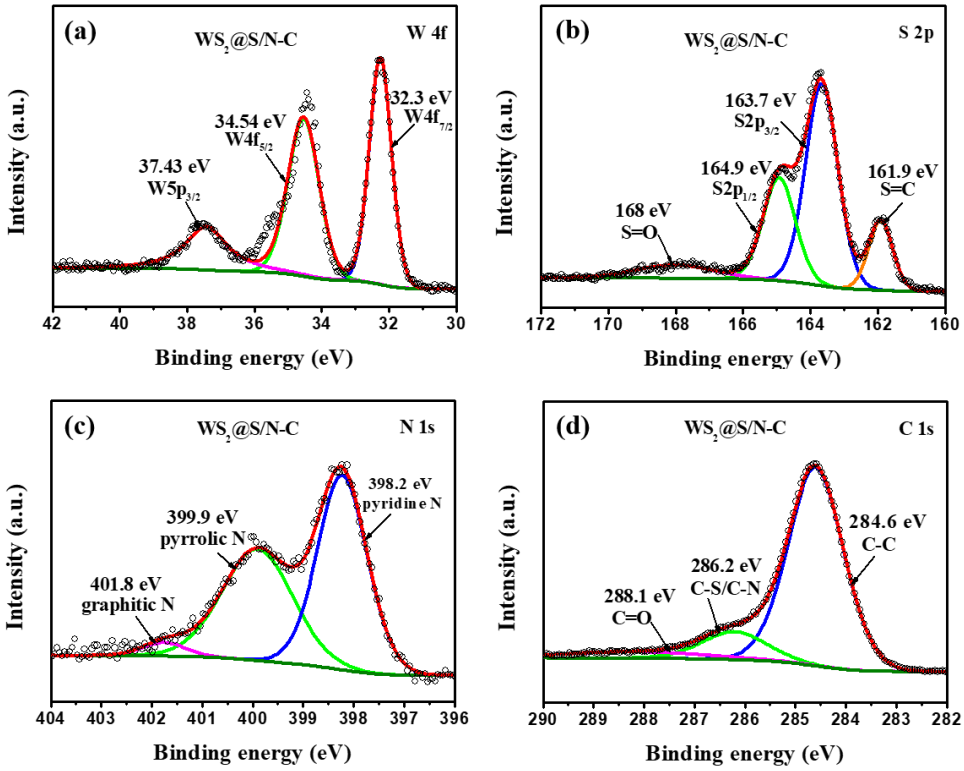

Figure 3 High-resolution XPS spectra of WS_2@S/N-C: (a) W; (b) S; (c) N; (d) C.

The chemical status of the WS_2@S/N-C and WS_2 samples was characterized by XPS (**Figure S5a)**. Compared to the spectrum of pure WS_2, the spectrum of WS_2@S/N-C reveals extra distinctive C and N peaks, which demonstrate successful doping in accordance with its FTIR spectrum. For WS_2@S/N-C, there are three strong peaks from W centered at 32.3, 34.54, and 37.43 eV, as shown in **Figure 3a**, which exhibit a shift to lower energy than for pure WS_2, the peaks of which are located at 33.1, 35.3, and 38.7 eV (**Figure S5b**), which might be associated with the interaction between WS_2 and C, N. There are two major peaks from S centered at 162.7 and 163.9 eV in pure WS_2 (**Figure S5c**), slightly shifted to lower energy than for the S peaks (163.7 and 164.9 eV) of WS_2@S/N-C (**Figure 3b**). Moreover, two shoulder peaks at 161.9 and 168.0 eV in **Figure 3b** are associated with S=C and S-O bonds in carbon nanofibers, indicating that S was successfully incorporated into the carbon matrix. Furthermore, there are three peaks at 398.2, 399.9, and 401.8 eV in the N 1s spectrum of WS_2@S/N-C (**Figure 3c**) indicate the existence of pyridinic, pyrrolic, and graphitic nitrogen in WS_2@S/N-C, respectively.[55] The pyrrolic and pyridinic nitrogen can give rise to surface defects in carbon structures that can offer channels to facilitate Na^+ diffusion.[5] In **Figure 3d**, the C 1s spectrum can be fitted into three peaks

for carbon atoms, including for C-C bonds (284.6 eV), C-S/C-N bonds (286.2 eV), and C=O bonds (288.1 eV). In consequence, it is clear that the nitrogen and sulfur dual-doping allows the Na^+ ions and electrons to achieve high transfer rates for good performance.[56]

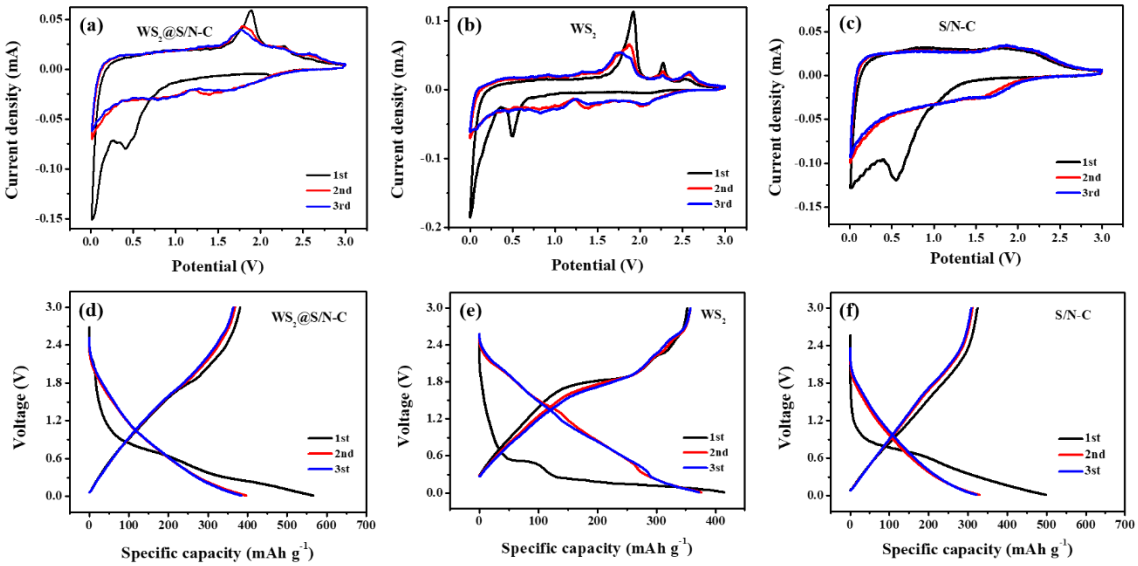

Figure 4 CV curves of (a) WS_2@S/N-C, (b) WS_2 and (c) S/N-C electrodes in the voltage range of 0.01-3 V at a scan rate of 0.1 mV s^{-1}; Charge–discharge profiles of (d) WS_2@S/N-C, (e) pure WS_2 and (f) S/N-C electrodes at a current density of 0.1 Ag^{-1}.

The electrochemical properties of the WS_2@S/N-C, WS_2 and S/N-C electrodes were characterized by CV and galvanostatic charge–discharge cycling. **Figure 4a-c** display the CV profiles of the WS_2@S/N-C nanofibers, pure WS_2 and S/N-C nanofibers for the initial 3 cycles at a scan rate of 0.1 m Vs^{-1}, respectively. For the WS_2@S/N-C electrode, the reduction peak centered at 0.5 V in the first cycle is attributed to the conversion reaction ($WS_2 + 4Na^+ + 4e^- \rightarrow W + 2Na_2S$) and the formation of an irreversible solid electrolyte interphase (SEI) film. In the following cycles, the reduction peak at ~0.5 V disappears while new reduction peaks appear in the potential range from 1.2 to 1.5 V, indicating the presence of reversible conversion mechanism ($4Na^+ + WS_2 + 4e^- \rightarrow W + 2Na_2S$). In the anodic scans, three peaks located at 1.8, 2.2, and 2.5 V are corresponded to the oxidation of W to WS_2 during the desodiation process.[33] Compared with the WS_2@S/N-C electrode, similar reduction and oxidation peaks were also observed for pure WS_2, although their variation was different from that of the WS_2@S/N-C electrode. For the S/N-C

electrode, a reduction peak centered at ~0.5 V in the first cycle is associated with the formation of an irreversible solid electrolyte interphase (SEI) film. The reduction and oxidation peaks of the WS_2@S/N-C and S/N-C electrodes show a much more stable profile and tend to overlap each other in the following two cycles, indicating faster Na^+ ion insertion/extraction kinetics and higher reversibility of the electrode reactions for WS_2@S/N-C and S/N-C electrodes. This confirmed the S/N-C nanofibers could stabilize the WS_2 during the electrochemical process. The charge/discharge curves of the WS_2@S/N-C nanofibers, pure WS_2 and S/N-C nanofibers in **Figure 4d-f** were collected at 0.1 Ag^{-1}. The WS_2@S/N-C nanofibers delivered a discharge and charge capacity of 566 and 381 mA h g^{-1} while pure WS_2 (416 and 352 mA h g^{-1}) and S/N-C nanofibers (465.8 and 356.9 mA h g^{-1}), respectively. Moreover, the coincidence of subsequent discharge/charge curves for pure WS_2@S/N-C, indicating a reversible and stable electrochemical performance.

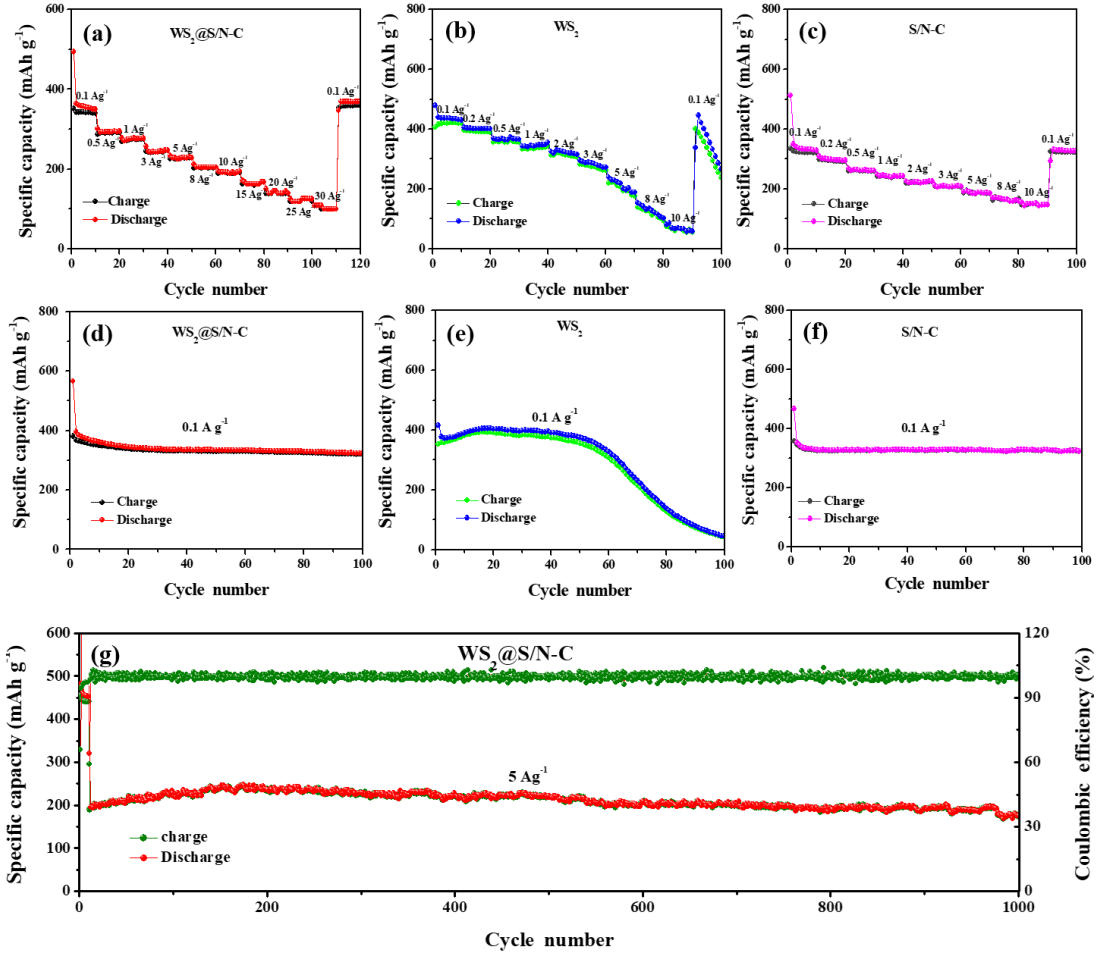

Figure 5 Rate capability of the (a) WS_2@S/N-C, (b) WS_2 and (c) S/N-C electrodes at various current densities; Cycling performance of the (d) WS_2@S/N-C, (e) WS_2 and (f) S/N-C electrodes

at a current density of 0.1 A g^{-1}; (g) Long-term cycling performance and Coulombic efficiency of WS_2@S/N-C electrode at a current density of 5 A g^{-1}.

Figure 5a shows the capacity of the WS_2@S/N-C electrode at various current densities from 0.1 to 30 A g^{-1}. The electrode delivers a reversible capacity of 371, 291, 275, 246, 230, 204, 192, 167, 145, and 125 mA h g^{-1} at current density of 0.1, 0.5, 1, 3, 5, 8, 10, 15, 20, and 25 A g^{-1}, respectively. Even at a very high current density of 30 A g^{-1}, it still delivers capacity of 108 mA h g^{-1} and when the current density returns to 0.1A g^{-1}, it keeps a reversible capacity of 360 mA h g^{-1}. The pure WS_2 electrode and S/N-C electrodes (**Figure 5b** and **c**), however, exhibits much poorer rate performance. The reversible capacity for the pure WS_2 electrode rapidly declines to 237 mA h g^{-1} when the current density returns to 0.1 A g^{-1}. The S/N-C electrode could keep a reversible capacity of 322.2 mA h g^{-1}, which is obviously lower than that of WS_2@S/N-C electrode. The excellent rate performance of WS_2@S/N-C can be attributed to its structure. The lotus rhizome-like carbon nanofibers could offer short paths to facilitate electron transfer, prevent pulverization of the electrode structure, and offer convenient Na^+ transport. Electrochemical impedance spectroscopy (EIS) was also carried out to study the reaction kinetics of WS_2@S/N-C and pure WS_2 electrode cycling after for 1 cycles at 0.1 A g^{-1}. In **Figure S6**, the WS_2@S/N-C electrode exhibits a much lower charge transfer resistance (R_{ct}, 298 Ω) than the pure WS_2 electrode (2129 Ω), based on the equivalent circuit simulation, which implies facile charge transfer at the electrode/electrolyte interface. Moreover, the discharge capacity of WS_2@S/N-C reached 319 mAh·g^{-1} at 0.1 A g^{-1} after 100 cycles (**Figure 5d**), showing good cycling stability. In comparison, the pure WS_2 only possessed 43 mA h·g^{-1}after 100 cycles (**Figure 5e**). The S/N-C can sustain 315 mA h g^{-1} after 100 cycles with good stability (**Figure 5f**). This demonstrates that S/N-C nanofibers facilitated the stability of WS_2. To further explain the difference in cycling stability between the two kinds of electrodes, the morphologies of cycled WS_2@S/N-C and pure WS_2 were characterized by SEM, as shown in **Figure S7**. Obviously, compared with fresh WS_2@S/N-C electrode, the surface of this electrode cycled after 100 cycles became less smooth due to the formation of solid electrolyte interphase (SEI). Although some small particles emerged, the rod-like morphology was partially maintained. On the contrary, the morphology of the WS_2 electrode cycled after 100 cycles changed significantly. No nanosheets could be observed. Based on above results, it was revealed that the different structural stabilities led to the different cycling

stabilities. Moreover, the WS_2@S/N-C even exhibited a capacity of 174 mA h·g^{-1} at a current of 5 A g^{-1} over 1000 cycles, with capacity retention of 89%, demonstrating excellent ultra-long cycling stability (**Figure 5g**).

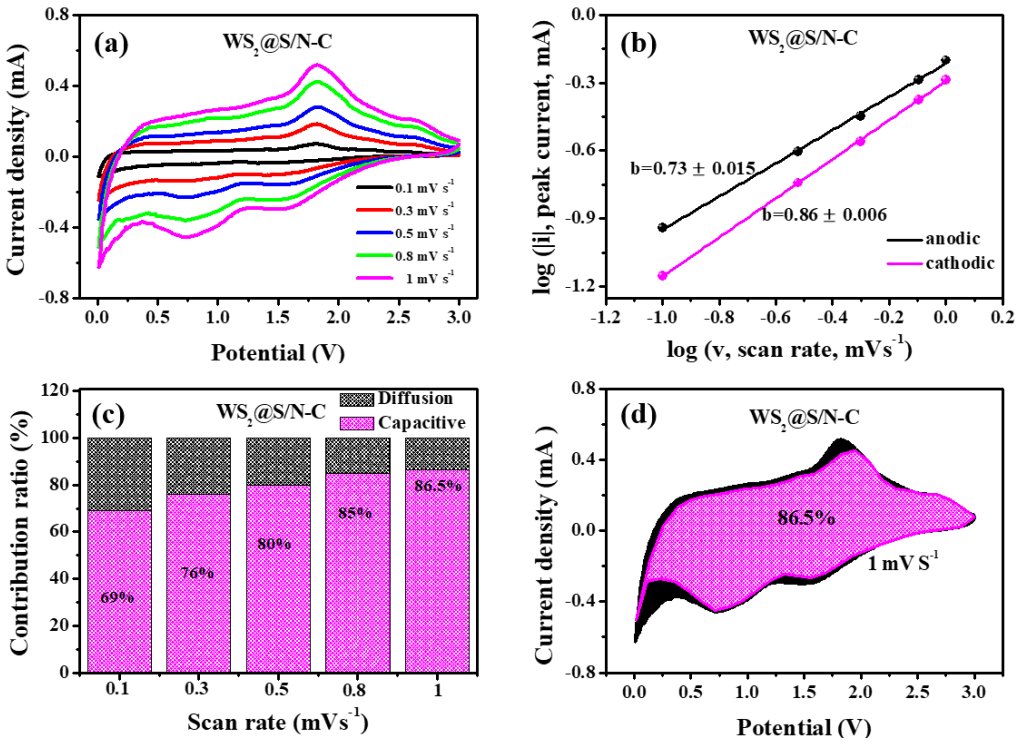

Figure 6 (a) CV curves of WS_2@S/N-C electrodes at different scan rates; (b) log *i* vs. log *v* plots of WS_2@S/N-C electrodes; (c) Ratio of diffusion and capacitive contributions to the capacity at various scan rates for WS_2@S/N-C electrodes; (d) Capacitive charge storage contribution (pink region) for WS_2@S/N-C electrode at 1.0 mV s^{-1}.

To further evaluate the electrochemical performance of WS_2@S/N-C anode, CV measurements at a series of scan rates from 0.1 mV s^{-1} to 1 mV s^{-1} were carried out. As displayed in **Figure 6a**, with the scan rates increasing, all the CV curves retained similar shapes with only a small deviation of the redox peaks, suggesting high rate capability and small potential polarization. As is well known, the electrochemical capacity is contributed by two mechanisms, the faradaic charge transfer process (ion diffusion) and the non-faradaic contribution (pseudocapacitance).[57] The relationship between peak current and scan rate can indicate the contribution of each part, as follows:[58]

$$i = av^b \quad (1)$$

and

$$log\ i = b\ log\ v + log\ a \quad (2)$$

where i represents the peak current, v is the scan rate, and a and b are adjustment parameters, respectively. The b value reveals the different types of charge storage. The values of 0.5 and 1 represent the faradaic charge transfer process and the non-faradaic contribution, respectively. In **Figure 6b**, the b values of WS_2@S/N-C anode were calculated to be 0.73 ± 0.015 for the anodic peaks and 0.86 ± 0.006 for the cathodic peaks, suggesting that the sodium storage reaction of WS_2@S/N-C anode was determined by both pseudocapacitive behavior and ion diffusion control. The percent contributions of the two parts at a serious of scan rates can be calculated from the following equation:

$$i = k_1v + k_2v^{1/2} \quad (3)$$

where k_1v represents the pseudocapacitive part and $k_2v^{1/2}$ represents the ion diffusion part. As can be seen from **Figure 6c**, the pseudocapacitive contribution increased from 69% to 86.5% as the scan rate increased from 0.1 mV s^{-1} to 1 mV s^{-1}. The detailed pseudocapacitive fraction at 1 mV s^{-1} is also illustrated in **Figure 6d**. These results mean that the pseudocapacitive contribution plays the major role in the overall capacity of the WS_2@S/N-C anode. This might be ascribed to the effect of S/N-C since there are more redox reactions in the surface of S/N-C.[5]

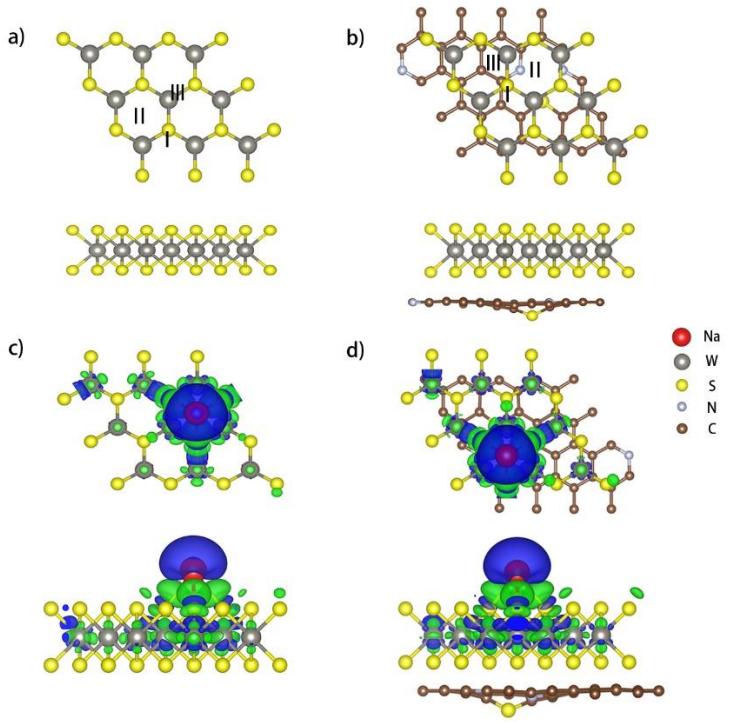

Figure 7 Adsorption sites for of I, II and III Na on (a) pure WS_2 and (b) the WS_2 in WS_2@S/N-C; Differences of charge density (charge accumulation: green, charge depletion: blue) with an isosurface level of 0.001 e/Å^3 for Na on (c) pure WS_2 and (d) the WS_2 in WS_2@S/N-C in the most stable adsorption configuration.

To obtain theoretical support for the results, we studied the Na^+ adsorption behavior on both pristine WS_2 surface and WS_2@S/N-C surface by DFT calculations. According to the previous theoretical calculations, the S/N co-doped graphene model can be as the S/N co-doped carbon nanofiber to analyze the adsorption behavior for the Li^+, Na^+ and K^+.[5, 59-63] Thus, we designed the heterostructure of WS_2 and S/N co-doped graphene to investigate the synergistic effects for Na adsorption. As shown in **Figure 7a** and **b**, both the pristine WS_2 and WS_2@S/N-C have three adsorption sites of S-top (Ⅰ), hollow (Ⅱ) and W-top (Ⅲ), respectively. And the adsorption energies of Na atom adsorption on pristine WS_2 and WS_2@S/N-C were calculated and illustrated in **Tables S1** and **S2**. For the S-top site, the adsorption energy of the Na in WS_2@S/N-C was -0.897 eV that was lower than that in pristine WS_2 (-0.494 eV). After the Na adsorption on the hollow site of pristine WS_2 and WS_2@S/N-C, the adsorption energies are of -0.744 eV and -1.168 eV, respectively. Clearly, the W-top site on WS_2@S/N-C has the smaller adsorption energy of -1.208 eV than that of pristine WS_2 (-0.759 eV). The smaller adsorption energies of Na adsorption on WS_2@S/N-C than that of pristine WS_2, indicating that WS_2@S/N-C is helpful for Na storage.

Moreover, we calculated the three-dimensional charge density difference to understand the mechanism of charge transfer on W-top site of pristine WS_2 or WS_2@S/N-C with a Na atom. As shown in **Figure 7c**, the charge accumulation is found on the W atoms, and the charge depletion appears on the Na ion at the same time. The results demonstrate that the charge has accumulated much more massively on the WS_2@S/N-C (**Figure 7d**) than on the pristine WS_2 (**Figure 7c**), which can be verified by the Bader charges. According to Bader charge analysis, 0.79 e of the Na atom is transferred onto the WS_2@S/N-C (**Table S2**), while only 0.76 e of the Na atom for the pristine WS_2 (**Table S1**). This shows that S/N-C could trap more Na atoms due to increasing the adsorption energy of the Na atom.

4. Conclusion

In conclusion, we have successfully realized the incorporation of WS_2 nanosheets into carbon nanofibers via an electrospinning/sulfidation process. Compared to pure WS_2, the WS_2@S/N-C nanofibers exhibit a higher rate capacity of 108 mA h g^{-1} at 30 A g^{-1} and a stable capacity of 174 mA h g^{-1} at 5 A g^{-1} after 1000 cycles. The theoretical studies demonstrate that S/N-C nanofibers effectively facilitate the storage of Na on WS_2. Moreover, analysis of the sodium storage mechanism has demonstrated that the capacitive contribution plays the dominant role in the whole capacity contribution owing to the S/N-heteroatom doping and the existence of the mesoporous defect-rich structure in the S/N-C matrix.

Conflicts of interest

There are no conflicts to declare.

Acknowledgements

The work was financially supported by an Australian Research Council (ARC) Linkage Project (DP160102627, DE170100928). We also thank Dr Tania Silver (University of Wollongong) for revising the manuscript.

References

1. Yabuuchi, N.; Kubota, K.; Dahbi, M.; Komaba, S., Research development on sodium-ion batteries. *Chem. Rev.* **2014,** *114* (23), 11636-82.
2. Christoph Vaalma, D. B., Marcel Weil and Stefano Passerini, A cost and resource analysis of sodium-ion batteries. *Nature Rev. Mater.* **2018,** *3*, 18013.
3. Fang, Y.; Yu, X.-Y.; Lou, X. W., Nanostructured electrode materials for advanced sodium-ion batteries. *Matter* **2019,** *1* (1), 90-114.
4. Nayak, P. K.; Yang, L.; Brehm, W.; Adelhelm, P., From lithium-ion to sodium-ion batteries: advantages, challenges, and surprises. *Angew. Chem. Int. Ed.* **2018,** *57* (1), 102-120.
5. Li, X.; Hu, X.; Zhou, L.; Wen, R.; Xu, X.; Chou, S.; Chen, L.; Cao, A.-M.; Dou, S., A S/N-doped high-capacity mesoporous carbon anode for Na-ion batteries. *J. Mater. Chem. A* **2019,** *7* (19), 11976-11984.
6. Cao, Y.; Xiao, L.; Sushko, M. L.; Wang, W.; Schwenzer, B.; Xiao, J.; Nie, Z.; Saraf, L. V.; Yang, Z.; Liu, J., Sodium ion insertion in hollow carbon nanowires for battery applications. *Nano Lett.* **2012,** *12* (7), 3783-3787.
7. Hou, H.; Banks, C. E.; Jing, M.; Zhang, Y.; Ji, X., Carbon quantum dots and their derivative 3D porous carbon frameworks for sodium-ion batteries with ultralong cycle life. *Adv. Mater.* **2015,** *27* (47), 7861-7866.
8. Lu, P.; Sun, Y.; Xiang, H.; Liang, X.; Yu, Y., 3D Amorphous carbon with controlled porous and disordered structures as a high-rate anode material for sodium-ion batteries. *Adv. Energy Mater.* **2018,** *8* (8) 1702434.
9. Ma, W.; Wang, J.; Gao, H.; Niu, J.; Luo, F.; Peng, Z.; Zhang, Z., A mesoporous antimony-based nanocomposite for advanced sodium ion batteries. *Energy Stor. Mater.* **2018,** *13*, 247-256.
10. Sheng, M.; Zhang, F.; Ji, B.; Tong, X.; Tang, Y., A Novel tin-graphite dual-ion battery based on sodium-ion electrolyte with high energy density. *Adv. Energy Mater.* **2017,** *7* (7), 1601963.
11. Yang, H.; Xu, R.; Yao, Y.; Ye, S.; Zhou, X.; Yu, Y., Multicore–shell Bi@N-doped carbon nanospheres for high power density and long cycle life sodium- and potassium-ion anodes. *Adv. Funct. Mater.* **2019,** *29* (13) 1809195.
12. Zhao, Y.; Manthiram, A., High-capacity, high-rate Bi-Sb alloy anodes for lithium-ion and sodium-ion batteries. *Chem. Mater.* **2015,** *27* (8), 3096-3101.
13. Chen, C.; Wen, Y.; Hu, X.; Ji, X.; Yan, M.; Mai, L.; Hu, P.; Shan, B.; Huang, Y., Na^+ intercalation pseudocapacitance in graphene-coupled titanium oxide enabling ultra-fast sodium storage and long-term cycling. *Nature Commun.* **2015,** *6*, 6929.
14. Zheng, Y.; Zhou, T.; Zhang, C.; Mao, J.; Liu, H.; Guo, Z., Boosted charge transfer in SnS/SnO_2 heterostructures: Toward high rate capability for sodium-ion batteries. *Angew. Chem. Int. Ed.* **2016,** *55* (10), 3408-13.
15. Chen, D.; Peng, L.; Yuan, Y.; Zhu, Y.; Fang, Z.; Yan, C.; Chen, G.; Shahbazian-Yassar, R.; Lu, J.; Amine, K.; Yu, G., Two-dimensional holey Co_3O_4 nanosheets for high-rate alkali-ion batteries: From rational synthesis to in situ probing. *Nano Lett.* **2017,** *17* (6), 3907-3913.
16. Zhang, K.; Park, M.; Zhou, L.; Lee, G.-H.; Li, W.; Kang, Y.-M.; Chen, J., Urchin-like $CoSe_2$ as a high-performance anode material for sodium-ion batteries. *Adv. Funct. Mater.* **2016,** *26* (37), 6728-6735.
17. Wang, Y.; Wang, Y.; Kang, W.; Cao, D.; Li, C.; Cao, D.; Kang, Z.; Sun, D.; Wang, R.; Cao, Y.,

TiO_2-coated interlayer-expanded $MoSe_2$/phosphorus-doped carbon nanospheres for ultrafast and ultralong cycling sodium storage. *Adv. Sci.* **2019,** *6* (1), 1801222.
18. Zhang, F.; Xia, C.; Zhu, J.; Ahmed, B.; Liang, H.; Velusamy, D. B.; Schwingenschlögl, U.; Alshareef, H. N., $SnSe_2$ 2D Anodes for advanced sodium ion batteries. *Adv. Energy Mater.* **2016,** *6* (22) 1601188.
19. Wang, S.; Xia, L.; Yu, L.; Zhang, L.; Wang, H.; Lou, X. W. D., Free-standing nitrogen-doped carbon nanofiber films: integrated electrodes for sodium-ion batteries with ultralong cycle life and superior rate capability. *Adv. Energy Mater.* **2016,** *6* (7) 1502217.
20. Li, W.; Zhou, M.; Li, H.; Wang, K.; Cheng, S.; Jiang, K., A high performance sulfur-doped disordered carbon anode for sodium ion batteries. *Energy Environ. Sci.* **2015,** *8* (10), 2916-2921.
21. Yang, J.; Zhou, X.; Wu, D.; Zhao, X.; Zhou, Z., S-doped N-rich carbon nanosheets with expanded interlayer distance as anode materials for sodium-ion batteries. *Adv. Mater.* **2017,** *29* (6), 1604108.
22. Li, Z.; Ding, J.; Mitlin, D., Tin and tin compounds for sodium ion battery anodes: phase transformations and performance. *Acc. Chem. Res.* **2015,** *48* (6), 1657-1665.
23. Ni, J.; Bi, X.; Jiang, Y.; Li, L.; Lu, J., Bismuth chalcogenide compounds Bi_2X_3 (X=O, S, Se): Applications in electrochemical energy storage. *Nano Energy* **2017,** *34*, 356-366.
24. Hu, Z.; Liu, Q.; Chou, S. L.; Dou, S. X., Advances and challenges in metal sulfides/selenides for next-generation rechargeable sodium-ion batteries. *Adv. Mater.* **2017,** *29* (48) 1700606.
25. Yang, D.; Chen, W.; Zhang, X.; Mi, L.; Liu, C.; Chen, L.; Guan, X.; Cao, Y.; Shen, C., Facile and scalable synthesis of low-cost FeS@C as long-cycle anodes for sodium-ion batteries. *J. Mater. Chem. A* **2019,** *7* (34), 19709-19718.
26. Fang, Y.; Yu, X.-Y.; Lou, X. W. D., Bullet-like Cu_9S_5 hollow particles coated with nitrogen-doped carbon for sodium-ion batteries. *Angew. Chem. Int. Ed.* **2019,** *58* (23), 7744-7748.
27. Zhang, Y.; Zhou, Q.; Zhu, J.; Yan, Q.; Dou, S. X.; Sun, W., Nanostructured metal chalcogenides for energy storage and electrocatalysis. *Adv. Funct. Mater.* **2017,** *27* (35), 1702317.
28. Yun, Q.; Lu, Q.; Zhang, X.; Tan, C.; Zhang, H., Three-dimensional architectures constructed from transition-metal dichalcogenide nanomaterials for electrochemical energy storage and conversion. *Angew. Chem. Int. Ed.* **2018,** *57* (3), 626-646.
29. Huang, J.; Wei, Z.; Liao, J.; Ni, W.; Wang, C.; Ma, J., Molybdenum and tungsten chalcogenides for lithium/sodium-ion batteries: Beyond MoS_2. *J. Energy Chem.* **2019,** *33*, 100-124.
30. Lim, Y. V.; Wang, Y.; Kong, D.; Guo, L.; Wong, J. I.; Ang, L. K.; Yang, H. Y., Cubic-shaped WS_2 nanopetals on a prussian blue derived nitrogen-doped carbon nanoporous framework for high performance sodium-ion batteries. *J. Mater. Chem. A* **2017,** *5* (21), 10406-10415.
31. Song, Y.; Liao, J.; Chen, C.; Yang, J.; Chen, J.; Gong, F.; Wang, S.; Xu, Z.; Wu, M., Controllable morphologies and electrochemical performances of self-assembled nano-honeycomb WS_2 anodes modified by graphene doping for lithium and sodium ion batteries. *Carbon* **2019,** *142*, 697-706.
32. Wang, Y.; Kong, D.; Huang, S.; Shi, Y.; Ding, M.; Von Lim, Y.; Xu, T.; Chen, F.; Li, X.; Yang, H. Y., 3D carbon foam-supported WS_2 nanosheets for cable-shaped flexible sodium ion batteries. *J. Mater. Chem. A* **2018,** *6* (23), 10813-10824.
33. Wang, Y.; Kong, D.; Shi, W.; Liu, B.; Sim, G. J.; Ge, Q.; Yang, H. Y., Ice templated free-standing hierarchically WS_2/CNT-rGO aerogel for high-performance rechargeable lithium

and sodium ion batteries. *Adv. Energy Mater.* **2016,** *6* (21) 1601057.
34. Choi, S. H.; Kang, Y. C., Sodium ion storage properties of WS_2-decorated three-dimensional reduced graphene oxide microspheres. *Nanoscale* **2015,** *7* (9), 3965-3970.
35. Su, D.; Dou, S.; Wang, G., WS_2@graphene nanocomposites as anode materials for Na-ion batteries with enhanced electrochemical performances. *Chem. Commun.* **2014,** *50* (32), 4192-4195.
36. Song, Y.; Bai, S.; Zhu, L.; Zhao, M.; Han, D.; Jiang, S.; Zhou, Y. N., Tuning pseudocapacitance via C-S bonding in WS_2 nanorods anchored on N,S codoped graphene for high-power lithium batteries. *ACS Appl. Mater. Interfaces* **2018,** *10* (16), 13606-13613.
37. Wang, X.; Huang, J.; Li, J.; Cao, L.; Hao, W.; Xu, Z., Improved Na storage performance with the involvement of nitrogen-doped conductive carbon into WS_2 Nanosheets. *ACS Appl. Mater. Interfaces* **2016,** *8* (36), 23899-23908.
38. Zeng, X.; Ding, Z.; Ma, C.; Wu, L.; Liu, J.; Chen, L.; Ivey, D. G.; Wei, W., Hierarchical nanocomposite of hollow N-doped carbon spheres decorated with ultrathin WS_2 Nanosheets for high-performance lithium-ion battery anode. *ACS Appl. Mater. Interfaces* **2016,** *8* (29), 18841-18848.
39. Pang, Q.; Gao, Y.; Zhao, Y.; Ju, Y.; Qiu, H.; Wei, Y.; Liu, B.; Zou, B.; Du, F.; Chen, G., Improved lithium-ion and sodium-ion storage properties from few-layered WS_2 nanosheets embedded in a mesoporous CMK-3 matrix. *Chemistry* **2017,** *23* (29), 7074-7080.
40. Xu, X. D.; Li, X. J.; Zhang, J. Q.; Qiao, K.; Han, D. Z.; Wei, S. T.; Xing, W.; Yan, Z. F., Surfactant assisted electrospinning of WS_2 nanofibers and its promising performance as anode material of sodium-ion batteries. *Electrochim. Acta* **2019,** *302*, 259-269.
41. Liang, J.; Wei, Z.; Wang, C.; Ma, J., Vacancy-induced sodium-ion storage in N-doped carbon nanofiber@MoS_2 nanosheet arrays. *Electrochim. Acta* **2018,** *285*, 301-308.
42. Wu, C.; Zeng, X.; He, P.; Chen, L.; Wei, W., Flexible WS_2 @CNFs membrane electrode with outstanding lithium storage performance derived from capacitive behavior. *Adv. Mater. Interfaces* **2018,** *5* (3) 1701080.
43. Zhou, S.; Chen, J.; Gan, L.; Zhang, Q.; Zheng, Z.; Li, H.; Zhai, T., Scalable production of self-supported WS_2 /CNFs by electrospinning as the anode for high-performance lithium-ion batteries. *Science Bulletin* **2016,** *61* (3), 227-235.
44. Yu, X.; Pei, C.; Chen, W.; Feng, L., 2 dimensional WS_2 tailored nitrogen-doped carbon nanofiber as a highly pseudocapacitive anode material for lithium-ion battery. *Electrochim. Acta* **2018,** *272*, 119-126.
45. Ma, J.; Zhang, J.; Wang, S.; Wang, T.; Lian, J.; Duan, X.; Zheng, W., Topochemical preparation of WO_3 nanoplates through precursor H_2WO_4 and their gas-sensing performances. *J. Phys. Chem. C* **2011,** *115* (37), 18157-18163.
46. Wei, Z.; Zhang, Y.; Wang, S.; Wang, C.; Ma, J., Fe-doped phosphorene for the nitrogen reduction reaction. *J. Mater. Chem. A* **2018,** *6* (28), 13790-13796.
47. Kresse, G.; Hafner, J., Ab initio molecular dynamics for liquid metals. *Phys. Rev. B* **1993,** *47* (1), 558-561.
48. Perdew, J. P.; Burke, K.; Ernzerhof, M., Generalized gradient approximation made simple *Phys. Rev. Lett.* **1996,** *77*, 3865.
49. Blöchl, P. E., Projector augmented-wave method. *Phys. Rev. B* **1994,** *50* (24), 17953-17979.
50. Kresse, G.; Joubert, D., From ultrasoft pseudopotentials to the projector augmented-wave

method. *Phys. Rev. B* **1999**, *59 (3)*, 1758.
51. Malard, L. M.; Pimenta, M. A.; Dresselhaus, G.; Dresselhaus, M. S., Raman spectroscopy in graphene. *Phys. Rep.* **2009,** *473* (5-6), 51-87.
52. Yu, X.-G.; Xie, J.-Y.; Yang, J.; Huang, H.-J.; Wang, K.; Wen, Z.-S., Lithium storage in conductive sulfur-containing polymers. *J. Electroanal. Chem.* **2004,** *573* (1), 121-128.
53. Piaggio, P; Cuniberti, C.; Dellepiane, G.; Campani, E.; Gorini, G.; Masetti, G.; M. Novi, M.; Petrillo, G., Vibrational spectra and assignment of poly-(p-phenylene sulfide) and its oligomers. *Spectrochim. Acta* **1989,** *45A (3)*, 347-356.
54. Ma, R.; Fan, L.; Wang, J.; Lu, B., Confined and covalent sulfur for stable room temperature potassium-sulfur battery. *Electrochim. Acta* **2019,** *293*, 191-198.
55. Tan, H.; Tang, J.; Zhou, X.; Golberg, D.; Bhatia, S. K.; Sugahara, Y.; Yamauchi, Y., Preparation of 3D open ordered mesoporous carbon single-crystals and their structural evolution during ammonia activation. *Chem. Commun.* **2018,** *54* (68), 9494-9497.
56. Fu, L.; Tang, K.; Song, K.; van Aken, P. A.; Yu, Y.; Maier, J., Nitrogen doped porous carbon fibres as anode materials for sodium ion batteries with excellent rate performance. *Nanoscale* **2014,** *6* (3), 1384-1389.
57. Xia, X.; Chao, D.; Zhang, Y.; Zhan, J.; Zhong, Y.; Wang, X.; Wang, Y.; Shen, Z. X.; Tu, J.; Fan, H. J., Generic synthesis of carbon nanotube branches on metal oxide arrays exhibiting stable high-rate and long-cycle sodium-ion storage. *Small* **2016,** *12* (22), 3048-58.
58. Augustyn, V.; Simon, P.; Dunn, B., Pseudocapacitive oxide materials for high-rate electrochemical energy storage. *Energ Environ. Sci.* **2014,** *7* (5).
59. Lei, W.; Xiao, W.; Li, J.; Li, G.; Wu, Z.; Xuan, C.; Luo, D.; Deng, Y. P.; Wang, D.; Chen, Z., Highly nitrogen-doped three-dimensional carbon fibers network with superior sodium storage capacity. *ACS Appl Mater Interfaces* **2017,** *9* (34), 28604-28611.
60. Yao, Y.; Xu, R.; Chen, M.; Cheng, X.; Zeng, S.; Li, D.; Zhou, X.; Wu, X.; Yu, Y., Encapsulation of SeS_2 into nitrogen-doped free-standing carbon nanofiber film enabling long cycle life and high energy density K-SeS_2 battery. *ACS Nano* **2019,** *13* (4), 4695-4704.
61. Cui, J.; Yao, S.; Ihsan-Ul-Haq, M.; Wu, J.; Kim, J.-K., Correlation between Li plating behavior and surface characteristics of carbon matrix toward stable Li metal anodes. *Adv. Energy Mater.* **2019,** *9* (1) 1802777.
62. Jin, T.; Li, H. X.; Li, Y.; Jiao, L. F.; Chen, J., Intercalation pseudocapacitance in flexible and self-standing V_2O_3 porous nanofibers for high-rate and ultra-stable K ion storage. *Nano Energy* **2018,** *50*, 462-467.
63. Wu, Y.; Hu, S.; Xu, R.; Wang, J.; Peng, Z.; Zhang, Q.; Yu, Y., Boosting potassium-ion battery performance by encapsulating red phosphorus in free-standing nitrogen-doped porous hollow carbon nanofibers. *Nano Lett.* **2019,** *19* (2), 1351-1358.

Supporting information

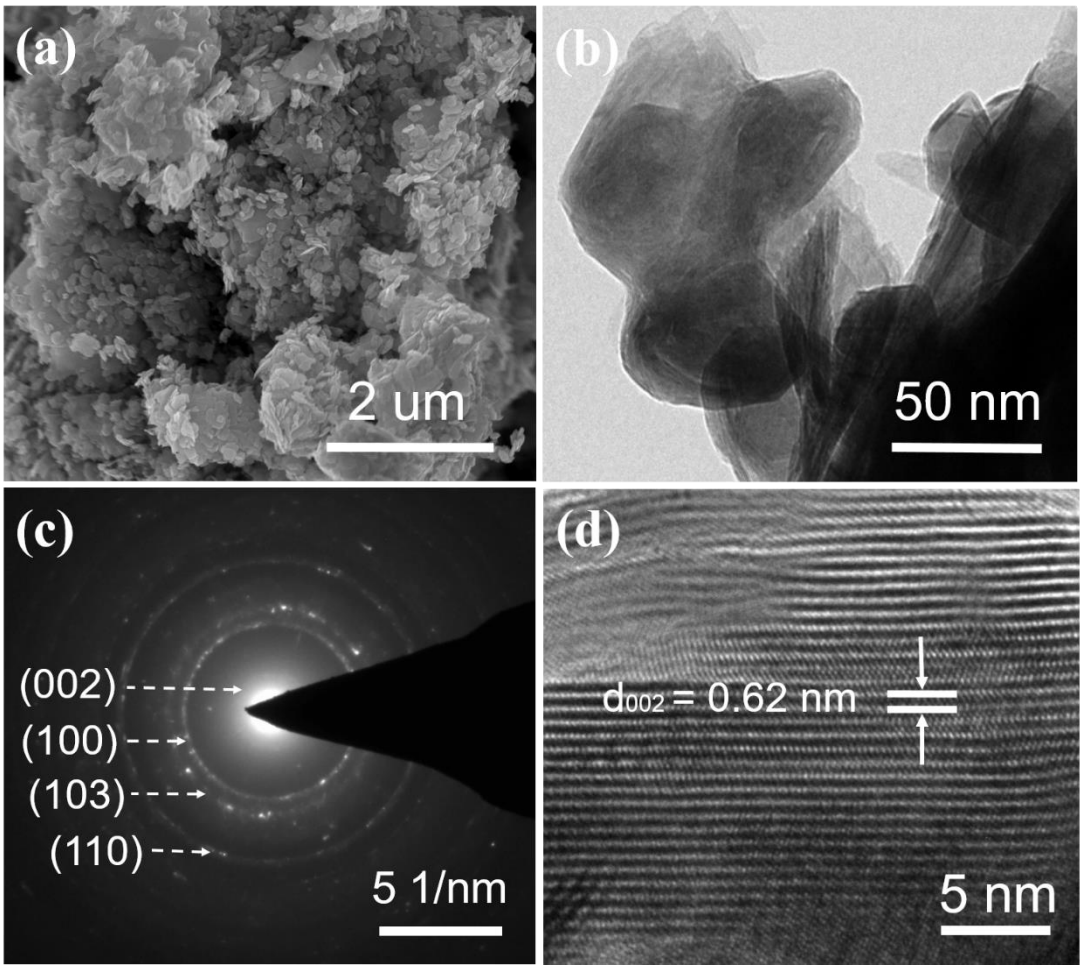

Figure S1 (a) low–resolution SEM image and (b) TEM image of pure WS_2; (c) electron diffraction pattern, and (d) high–resolution TEM image of pure WS_2.

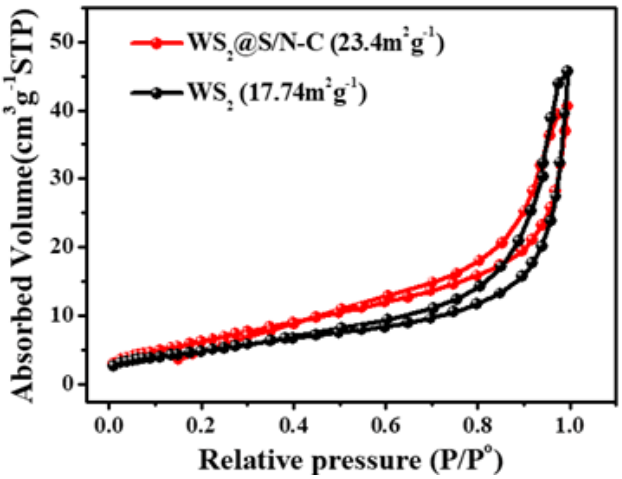

Figure S2 Nitrogen adsorption and desorption isotherms of WS_2@S/N-C nanofibers and pure WS_2.

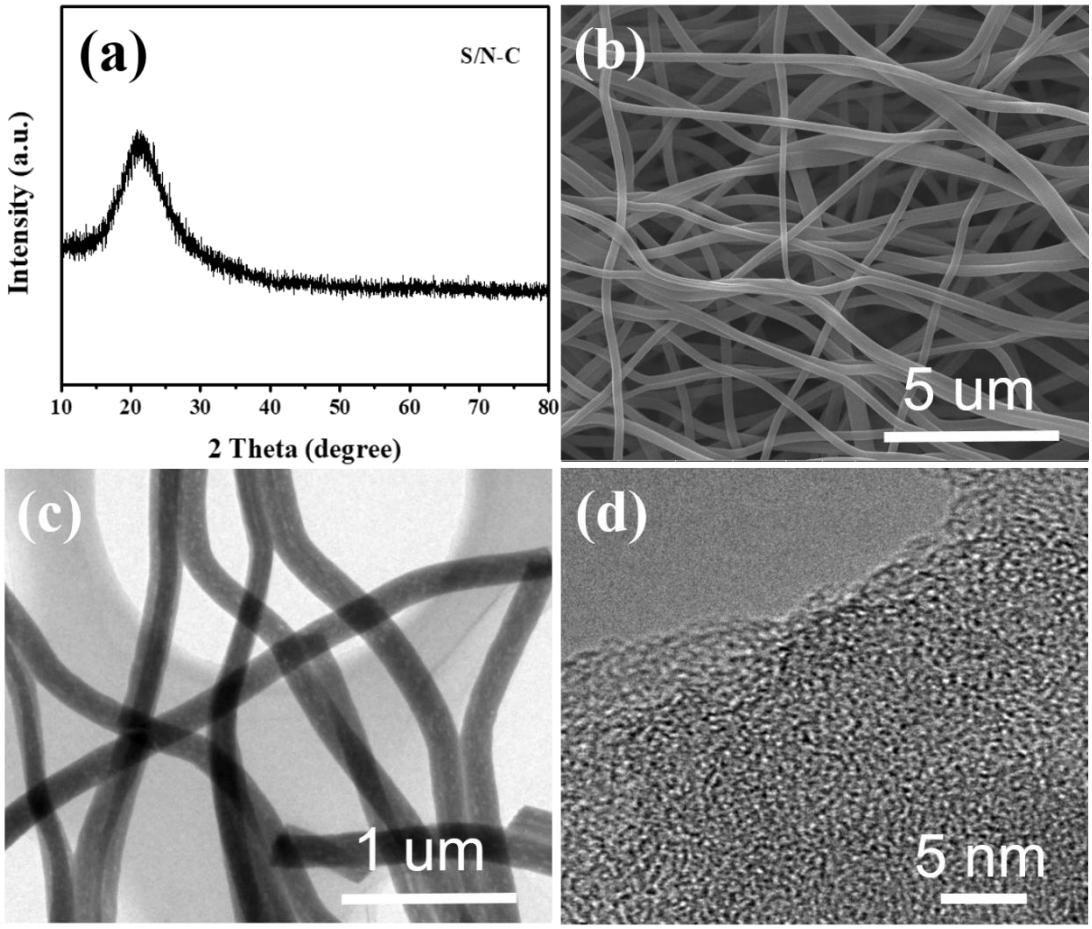

Figure S3 Characterizations of S/N-C nanofibers: (a) XRD pattern; (b) SEM image; (c) TEM image and (d) HR-TEM image.

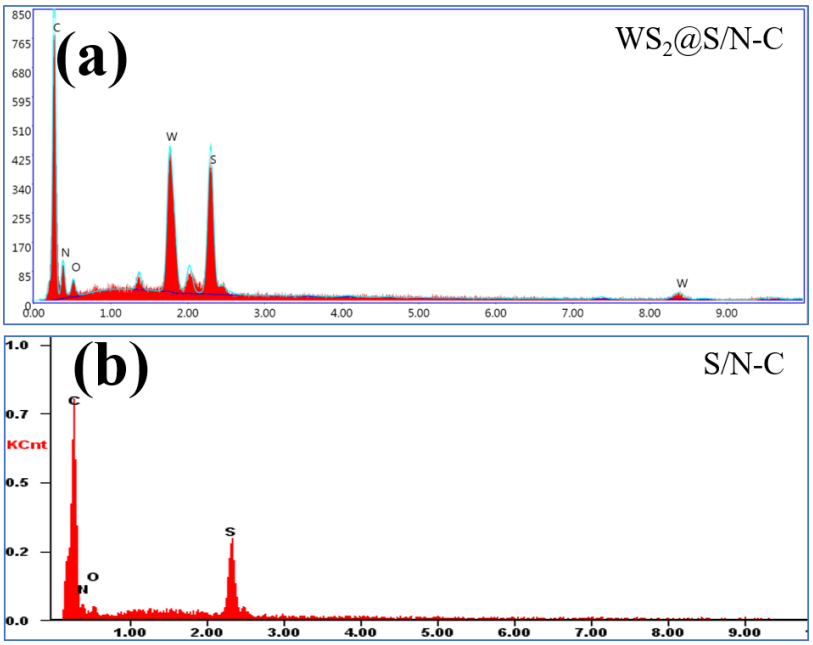

Figure S4 EDS spectrum of (a) WS_2@S/N-C nanofibers and (b) S/N-C nanofibers.

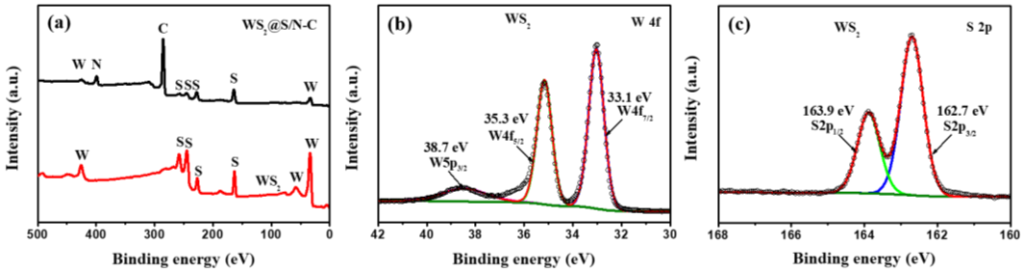

Figure S5 (a) XPS full survey spectra of WS_2@S/N-C nanofibers and pure WS_2; (b and c) High-resolution XPS spectra of W and S elements for pure WS_2.

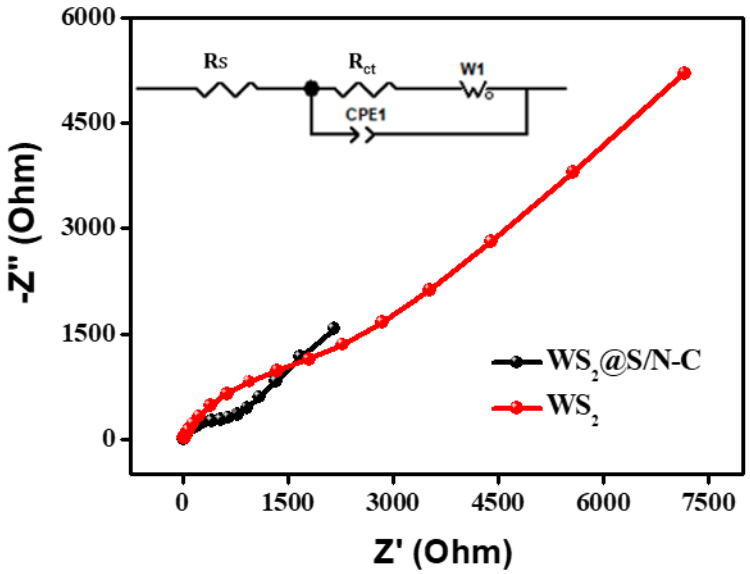

Figure S6 EIS spectra for WS_2@S/N-C and pure WS_2 after cycling for 1 cycle at 0.1 A g^{-1}. The inset is the equivalent circuit.

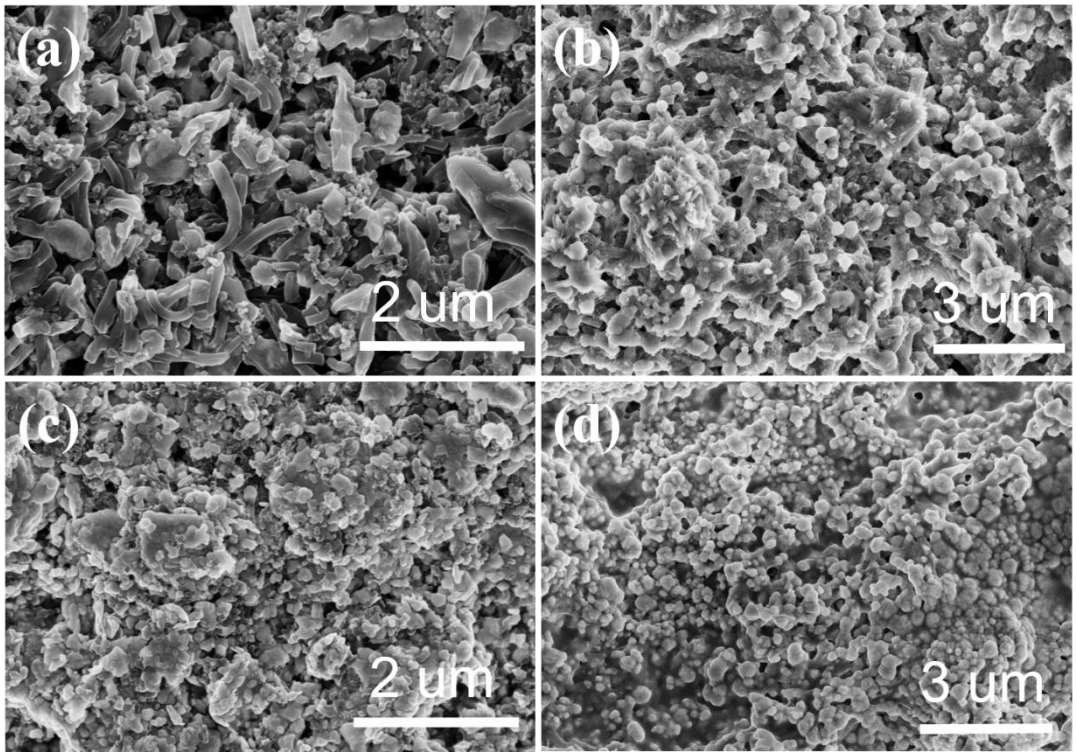

Figure S7 Low–resolution SEM images of WS_2@S/N-C electrode: (a) fresh electrode and (b) cycled electrode after 100 cycles; low–resolution SEM images of WS_2 electrode: (c) fresh electrode and (d) cycled electrode after 100 cycles.

Table S1. The adsorption behavior of Na on pristine WS_2.

Adsorption sites / WS_2	Ⅰ (S-top)	Ⅱ (Hollow)	Ⅲ (W-top)
E_{ad} (eV)	-0.494	-0.744	-0.759
Q_{Na} (|e|)	0.56	0.74	0.76

Table S2. The adsorption behavior of Na on WS_2@S/N-C.

Adsorption sites / WS_2@S/N-C	Ⅰ (S-top)	Ⅱ (Hollow)	Ⅲ (W-top)
E_{ad} (eV)	-0.897	-1.168	-1.208
Q_{Na} (|e|)	0.65	0.79	0.79